Satellite-derived shoreline detection at a high-energy meso-macrotidal beach

Bruno Castelle, Gerd Masselink, Tim Scott, Christopher Stokes, Aikaterini Konstantinou, Vincent Marieu, Stéphane Bujan

HAL Id: hal-03411192

https://hal.science/hal-03411192

Submitted on 2 Nov 2021

1   **Satellite-derived shoreline detection at a high-energy meso-macrotidal beach**

2   Bruno Castelle[1,2], Gerd Masselink[3], Tim Scott[3], Christopher Stokes[3], Aikaterini Konstantinou[3], Vincent

3   Marieu[1,2], Stéphane Bujan[1,2]

4   [1]CNRS, UMR EPOC, Pessac, France

5   [2]Université de Bordeaux, UMR EPOC, Pessac, France

6   [3]Coastal Processes Research Group, School of Biological and Marine Sciences, University of Plymouth,

7   Plymouth, UK

8   Corresponding author: bruno.castelle@u-bordeaux.fr

9

10   **Highlights**

11   • 35 years of satellite-derived shorelines at a high-energy tidal beach are analysed

12   • Satellite-derived shoreline proxies are compared with 10 years of field data

13   • A new approach using wave runup and a threshold on total water level is proposed

14   • The approach halves shoreline error and doubles the number of usable images

15   **Abstract**

16   Publicly available satellite imagery can now provide multi-decadal time series of shoreline data from

17   local to global scale, enabling analysis of sandy beach shoreline variability across a spectrum of

18   temporal scales. Such data can, however, be associated with large uncertainties, particularly for

19   beaches experiencing a large tidal range (> 2 m) and energetic incident waves. We use a decade of bi-

20   monthly topographic surveys at the high-energy meso-macrotidal beach of Truc Vert, southwest

21   France, and concurrent wave and water-level hindcast to investigate the uncertainties associated

22   with satellite-derived time series of the shoreline position. We show that consideration of the water

23   level and wave runup elevation are critical for accurately estimating waterline position and, in turn,

24   shoreline position. At Truc Vert, including non-tidal water level residuals (e.g. wind-driven surge) and

25   accounting for time- and elevation-varying beach slope for horizontal correction did not improve

26   satellite-derived shoreline position. A new total water level threshold is proposed to maximize the

27   number of usable images while minimizing errors. Accounting for wave runup and the new water

28   level threshold at Truc Vert, the number of usable satellite images is doubled and shoreline position

29   errors are at least halved compared to previous work at this site. Using the 1984-2019 reconstructed

30   shoreline, we also show that the satellite-derived shoreline trends and interannual variability are in

31   better agreement with field measurements. Although the approach proposed here needs to be

32   tested on other sites in different tidal/wave forcing environments with different morphological and

33   sediment characteristics, we anticipate that it will improve the temporal and spatial description of

34   shoreline change on most surf tidal beaches where accurate continuous water level and wave

35   hindcasts and/or observations are available.

36   **Keywords:** shoreline change; long-term trend; satellite; wave runup

37

38

1. Introduction

Understanding and predicting shoreline change along sandy coasts is of paramount importance for coastal managers and policy-makers (Stive et al., 2002). Ambient (or background) long-term shoreline change is an essential and sometimes dominant component in models of future shoreline change due to sea-level rise (Vitousek et al., 2017; Vousdoukas et al., 2020; McCarroll et al., 2020). However, shoreline variability occurs across a wide range of time scales and it can be challenging to derive the ambient shoreline change unless very long data time series are available. Shorelines can dramatically erode within hours as a result of storm waves (Harley et al., 2017). At the other end of the spectrum, long-term, multi-decadal shoreline change is driven by various processes such as sea-level rise (Ranasinghe et al., 2012) and coastal sediment supply (Carter et al., 1987). In between, seasonal and interannual shoreline variability is primarily driven by changes in incident wave conditions (Dodet et al., 2019); however, in sectors adjacent to tidal inlets and estuary mouths, fluctuations in ebb-channel morphology can also drive shoreline variability (O'Connor et al., 2011). Anthropogenic forcing, such as beach nourishments or implementation of hard structures that disturb sediment pathways may also have a profound impact on shoreline variability (Turner, 2006). A core issue to improve our understanding and ability to predict shoreline change is therefore to monitor shoreline change at the highest possible frequency and the longest possible time scale on a large range of sandy environments representative of the natural variability (Splinter et al., 2013; Ibaceta et al., 2020; Toimil et al., 2020).

There is a wealth of coastal monitoring techniques employed to survey beach morphology and derive shoreline change. These topographic surveys are often performed by means of GNSS surveys (Baptista et al., 2008). Large-scale GNSS coastal monitoring programs based on widely spaced beach profiles adequately distributed along 10s to 100s kilometres are scarce (Wijnberg and Terwindt, 1995; Ludka et al., 2019). Instead, most coastal monitoring programs focus on a single site through representative profiles (e.g., Lee et al., 1998; Suanez et al., 2012; Turner et al., 2016) or detailed digital elevation models (DEMs) along 100s to 1000s of metres (e.g., Stokes et al., 2015; Castelle et al., 2017a), which are typically surveyed monthly or bimonthly. On similar lengths of coastline, the daily shoreline proxy can be inferred from permanent video stations at reasonably low cost over years to decades (e.g., Harley et al., 2011), although associated with lower accuracy. Photogrammetry based on UAV images has also recently emerged as a promising tool to monitor 100s to 1000s metres of coast at high spatial resolution (e.g., Laporte-Fauret et al., 2019). Larger scale, say 10s to 100s of kilometres, coastal monitoring programs are typically based on Lidar surveys

71 (Le Mauff et al., 2018; Nicolae Lerma et al., 2019). However, such surveys are costly and have low

72 repeat frequencies. They are therefore difficult to maintain on the long-term and do not provide

73 insight into seasonal variability.

74 Publicly available satellite imagery can now be used at no cost to provide short-term to multi-decadal

75 shoreline data from local to global scale using a variety of techniques (e.g., Garcia-Rubio et al., 2015;

76 Liu et al., 2017; Qiao et al., 2018; Douarte et al., 2018; Toure et al., 2019). Long-term (> 30 yrs) global

77 estimation of shoreline erosion and accretion were recently proposed by Luijendijk et al. (2018) and

78 Mentaschi et al. (2018). Although these studies provided unprecedented global insight into shoreline

79 change, a detailed inspection of the satellite-derived trends computed in Luijendijk et al. (2018) at

80 many high-energy and/or meso to macrotidal beaches reveals that many of these trends are not

81 supported by field data and empirical evidence. Although trends appear reliable in sectors where

82 dramatic change is observed (Luijendijk et al., 2018), the discrepancies are obvious primarily in slowly

83 evolving sectors, say less than several metres per year, and at sites with a large intra- and inter-

84 annual shoreline variability. A more accurate assessment of shoreline change rates is therefore a

85 necessary requirement to develop reliable identification of a global typology of accreting, stable and

86 eroding shores. Furthermore, these computed historical trends can be extrapolated and combined

87 with debatable sea-level-rise impact rule to conclude on shoreline position by the end of the century

88 and potential extinction of half of the world's beaches (Vousdoukas et al., 2020). In addition to

89 addressing the limitations to this approach pointed out in Cooper et al. (2020), such pioneering

90 projective work would gain in reliability by improving the historical shoreline trends, as well as

91 including the effects of potential multi-decadal variability.

92 Vos et al. (2019a) recognised issues with detecting shorelines using satellite data on dissipative

93 beaches and sites experiencing a large tidal range. After Liu et al. (2017) who showed that tidal effect

94 correction improves satellite-derived shoreline errors, Vos et al. (2019b) tested a tidal correction at a

95 meso-macrotidal site by using a time-invariant characteristic beach face slope and only using images

96 captured at higher stages of the tide. This decreased the shoreline position error by 15 m. No

97 significant improvement in their error statistics was found using slope measurements from the

98 closest survey compared to using the single time-invariant slope value. However, the effects of wave

99 runup on water level at the coast, which can cause large horizontal translation of the waterline and

100 shoreline position under moderate- to high-energy breaking waves, was not considered. Other

101 sources of errors associated with satellite-derived shorelines can also arise, such as for instance

102 through issues with geo-referencing (Schubert et al., 2017) and incorrect delineation of the

103 water/sand interface (Toure et al., 2019).

104 Overall, improving satellite-derived shoreline positions and, in turn, shoreline trends is critical to
105 more accurately discriminate accreting, stable and eroding beaches, and to reduce uncertainties in
106 future shoreline change projections in the frame of climate change, both locally and globally. In this
107 paper, we address satellite-derived shoreline evolution at the high-energy and meso-macrotidal
108 beach of Truc Vert, southwest France, using the out-of-the-box open access python-based CoastSat
109 toolkit (Vos et al., 2019a, 2019b). We explore if including astronomical tide, non-tidal water level
110 residuals, wave action and local beach slope can reduce shoreline position uncertainties, and
111 therefore lead to an improved assessment of long-term trends and interannual variability. We also
112 investigate the value of increasing the number of satellite images in the analysis. These results have
113 strong implications from the perspective of global long-term trend computations and further
114 extrapolation until the end of the century, as well as for the assessment of interannual shoreline
115 variability on beaches.

116 **2. Study area**

117 The study site is located in southwest France, extending c. 140 km from the Gironde estuary in the
118 north to Biscarrosse in the south, with a focus on Truc Vert beach (Figure 1a). This sandy coast
119 comprises a large beach-dune system that is only interrupted by the Arcachon lagoon inlet.

120 The wave climate at these latitudes along the Atlantic coast of Europe is generated in the North
121 Atlantic Ocean, predominantly by eastward-tracking extra-tropical cyclones. Wave conditions at Truc
122 Vert, described below, are based on a numerical wave hindcast detailed in Section 3.2. The incident
123 wave conditions are strongly seasonally modulated with the monthly-averaged significant wave
124 height H_s, peak wave period T_p and angle of wave incidence θ ranging, respectively, from 1.1 m, 8.8 s
125 and 297° in summer, to 2.4 m, 12.1 s and 287° in winter (Figure 2a–c). Thus, larger and longer waves
126 with a more western incidence occur in winter compared to summer. Winter wave activity shows a
127 strong interannual variability, with moderate winters alternating with extreme winters characterised
128 by significant spatial and temporal storm clustering (Masselink et al., 2016). High-energy winters
129 occur as a result of the intensification and southward shift of Azores high / Icelandic low dipole,
130 which is strongly correlated with the West Europe Pressure Anomaly climate index and weakly
131 associated with the North Atlantic Oscillation (Castelle et al., 2017b).

132 The coast is meso-macrotidal with an annual mean spring tidal range of 3.7 m and a largest
133 astronomical tidal range of c. 5 m (Castelle et al., 2017a). Nearshore tide-driven currents are intense
134 (> 1 m/s) in the vicinity of the Gironde estuary mouth and Arcachon tidal inlet, and are negligible (<
135 0.2 m/s) compared to wave-driven currents on the open coast that can well exceed 1 m/s in rip-cell
136 circulation of under energetic obliquely incident waves.

137 The beach sediment consists of medium quartz sand with a median grain size of c. 0.35 mm and a

138 large spatial variability (Gallagher et al., 2011). Except adjacent to the tidal inlet and estuary mouths,

139 beaches are morphodynamically intermediate, but with a double-bar system. The subtidal outer bar

140 is modally crescentic and a modally transverse bar-rip system characterises the intertidal inner bar

141 system. The inner and outer mean rip spacing is approximately 400 and 700 m, respectively, with

142 large spatial and temporal variability (Castelle et al., 2007; Almar et al., 2010).

143 Analysis of georeferenced aerial photographs since 1950 showed a large spatial variability of

144 shoreline change within the study area (Castelle et al., 2018). Maximum shoreline dynamics are

145 observed along the sectors adjacent to the Gironde Estuary mouth and Arcachon inlet (Figure 1a),

146 with erosion and accretion alternating on the timescale of decades. In the northern sector near Cape

147 Négade (Figure 1a), the mean erosion rate is largest at c. 5 m/yr, with a quasi-steady trend. Mean

148 erosion rate decreases southwards to 1–2 m/yr at approximately 30 km south of Hourtin (Figure 1a).

149 Further south, the coast has been relatively stable over the last 70 years along a c. 20-km long sector.

150 This sector comprises Truc Vert beach (Figure 1a), of which topographic data will be used herein to

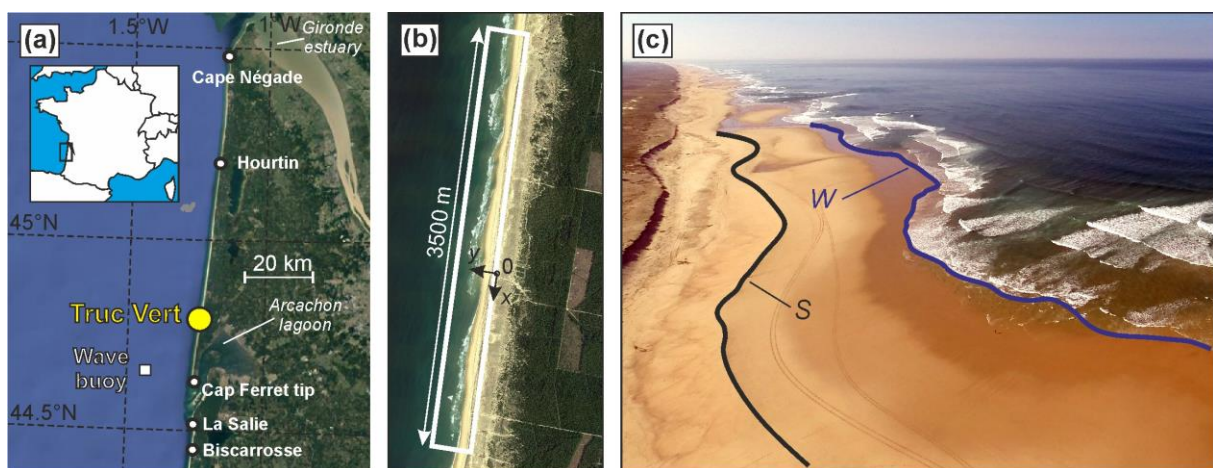151 compare satellite-derived shoreline dynamics.

152

153 Figure 1. (a) Location map, (b) survey region and reference frame used at Truc Vert beach and (c)

154 aerial view of Truc Vert beach taken between low and mid tide, with indication of water level (*W*)

155 position and visual estimate of the 1.5-m shoreline proxy *S*, which is the optimal shoreline proxy at

156 Truc Vert (photo: Vincent Marieu).

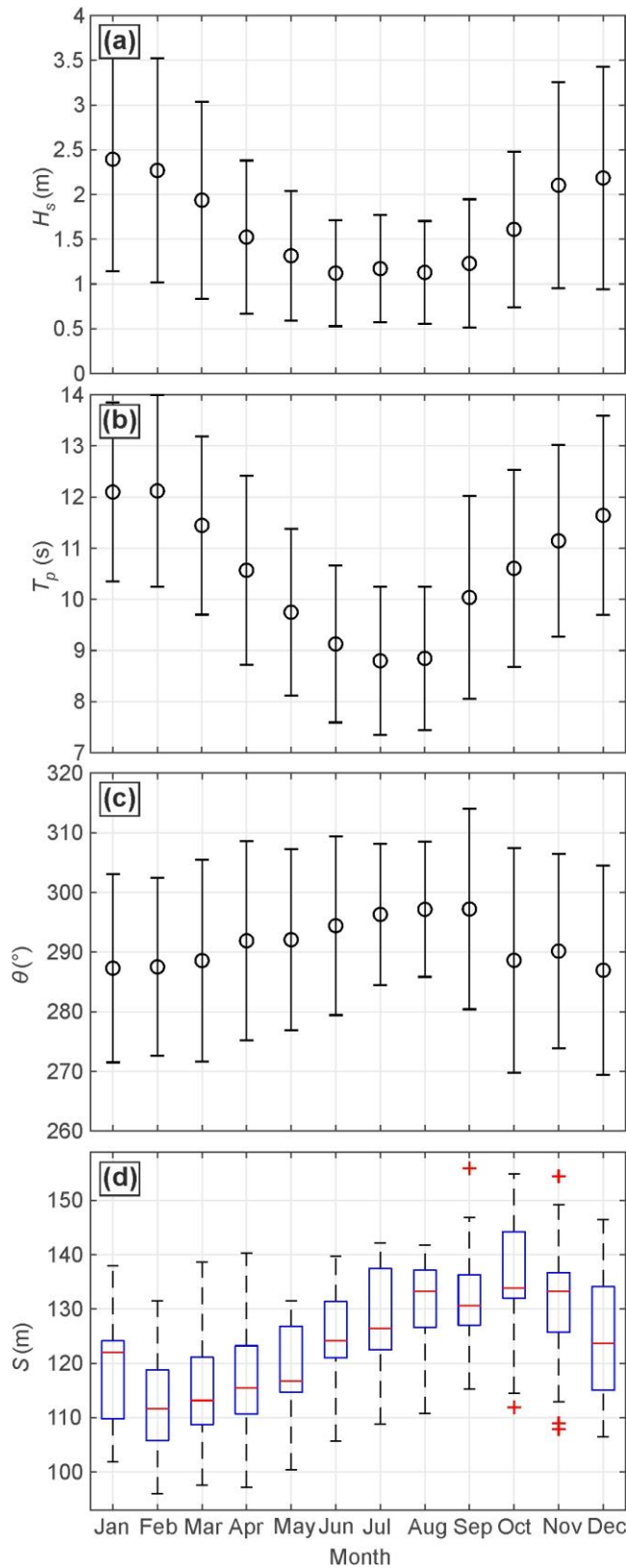Figure 2. Monthly wave statistics offshore of Truc Vert for 2005–2020: (a) significant wave height H_s; (b) peak wave period T_p; (c) angle of wave incidence θ; and (d) cross-shore position of the alongshore-averaged 1.5-m elevation shoreline proxy at Truc Vert S. Circles and vertical error bars in (a–c) indicate the monthly mean and the $\pm$ 1 monthly standard deviation, respectively. The central

162 horizontal mark in (d) indicates the median and the top and bottom edges of the blue boxes indicate

163 the 25th and 75th percentiles, respectively. Maximum whisker length extends up to 1.5 times the

164 interquartile range. Data points beyond these whiskers are considered as outliers and are displayed

165 individually as red crosses.

166 **3. Data and methods**

167 **3.1** *Truc Vert beach surveys*

168 A continuous beach survey program has been operational since 2003 at Truc Vert. The resulting

169 monthly to bi-monthly beach morphology dataset is detailed and made available in Castelle et al.

170 (2020). The alongshore coverage of the surveys increased over time, exceeding 600 m in 2009 before

171 stabilizing at c. 2200 m since early 2016 (Figure 3b). Figure 3c shows the time series of 1.5-m

172 elevation shoreline proxy cross-shore position $S_{1.5m}$, which has been used as the primary shoreline

173 proxy in previous studies (e.g., Castelle et al., 2014; Splinter et al., 2014) as it best correlates with the

174 beach-dune volume (Robinet et al., 2016). It is defined as the intersection of the alongshore-

175 averaged profile with the 1.5-m AMSL elevation datum, where AMSL is obtained at Truc Vert by

176 substracting 0.4 m from the French National Geodesic Service (NGF-IGN 69) height (Castelle et al.,

177 2020). In line with earlier work (e.g., D'Anna et al., 2020), the shoreline shows large seasonal cycles

178 with a typical amplitude of c. 30–40 m, with superimposed interannual variability of similar

179 amplitude. In the following, only the topographic data collected from 2009 onwards, which extend

180 more than 600 m alongshore, will be used for validation of local and alongshore-averaged satellite-

181 derived waterline ($\bar{X}$) and shoreline ($\bar{S}$) positions.

182

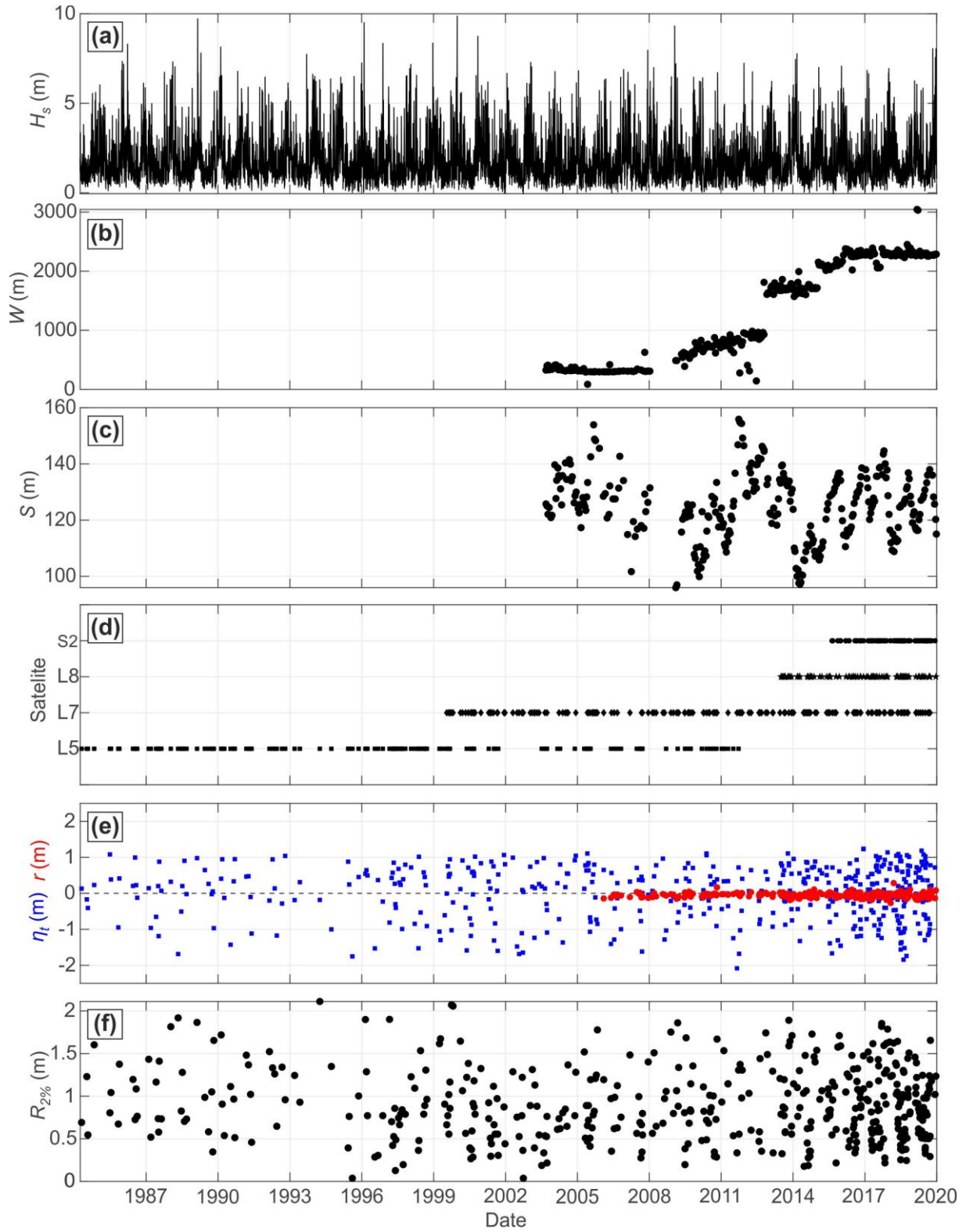Figure 3. Time series of: (a) significant wave height H_s; (b) survey alongshore coverage W; (c) cross-

shore location of the alongshore-averaged 1.5-m elevation shoreline proxy S computed from the

topographic surveys; (d) usable L5, L7, L8 and S2 satellite images after automatic and visual

inspection (see text for details); (e) astronomical tide η_t estimated from an harmonic analysis of

187   2006-2020 MARC hindcast, for which non-tidal residuals r were also extracted; and (f) runup

188   elevation $R_{2\%}$. All values shown in (e,f) are given at the satellite flyover time.

189   **3.2** *Wave and water level data*

190   There is no continuous wave buoy measurements nearby Truc Vert covering the 1984-2019 satellite

191   image period. Instead we used a 26-year (1994–2019) time series of regional wave hindcast

192   (Boudière et al., 2013; Michaud et al., 2015) at the grid point collocated with the Candhis directional

193   wave buoy moored in c. 54 m depth southwest of Truc Vert (Figure 1a), showing excellent skill

194   against interspersed buoy measurements (see Castelle et al., 2020 for details). To further extend the

195   time series from 1994 back until the early 1980s when the first satellite images were acquired, we

196   used the 1948–2015 wave hindcast described in Masselink et al. (2016), which was validated against

197   the nearby Candhis wave buoy data in Castelle et al. (2014), although with poorer skill than with the

198   1994-2019 regional wave model.

199   A 2006-2020 coastal model hindcast of water level (Pineau Guillou, 2013) validated at Truc Vert in

200   Castelle et al. (2020) was used to estimate the water level at the coast. The astronomical tide

201   component (η_t) as well as the water level including non-tidal (atmospheric) residuals r ($\eta_{ts} = \eta_t + r$)

202   were extracted all along the coast in c. 10 m depth. A harmonic analysis of the 2006-2020 MARC

203   hindcast astronomical tide (no storm surge) was performed to extend the time series of η_t back until
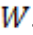
204   the early 1980s (Figure 3e).

205   Breaking waves are responsible for increased water level at the shoreline (Stockdon et al., 2006). We

206   tested many set-up ζ and runup $R_{2\%}$ parametrizations, which will be discussed later in the paper.

207   Based on preliminary tests and practical considerations, we used the runup formulation of Sénéchal

208   et al. (2011), specifically calibrated at Truc Vert:

209                               $$R_{2\%} = 2.14 \, \tanh 0.4 H_s \qquad (1)$$

210   Contrary to many other runup parametrizations (e.g., Stockdon et al., 2006), Equation (1) implies that

211     $R_{2\%}$ can be scaled using offshore wave height alone at Truc Vert. This is in line with previous

212   observations on highly dissipative beaches (Ruessink et al., 1998; Ruggiero et al., 2001) when

213   infragravity energy dominates runup.

214   Given that we also considered disregarding any water level variation ($\eta = \eta_0 = 0$), in total four

215   combinations of water level η at the coast were considered: no water level variation (η_0);

216   astronomical tide (η_t); astronomical tide + surge (η_{ts}); astronomical tide + surge + runup (η_{tsr}).

217   **3.3** *Publicly available satellite images and waterline detection algorithm*

218   We used the python toolkit CoastSat (Vos et al., 2019b) which is freely-available on GitHub
219   (https://github.com/kvos/CoastSat). The overall approach is described in detail in Vos et al. (2019a).
220   Briefly, the toolkit allows extracting waterlines from publicly available optical satellite data through
221   Google Earth Engine. Landsat 5, 7 & 8 (L5, L7, L8, 30-m spatial resolution) and Sentinel-2 (S2, 10-m
222   spatial resolution) images are retrieved to a user-defined region of interest before pre-processing to
223   remove cloudy pixels and enhance spatial resolution. A generic waterline detection algorithm is then
224   applied, consisting of two main steps: (1) an image classification into the four classes of 'sand',
225   'water', 'white-water' and 'other' is performed based on a Neural Network classifier algorithm
226   trained on five training sites along the New South Wales coast; and (2) a sub-pixel resolution border
227   segmentation based on the Modified Normalized Difference Water Index (MNDWI), which is widely
228   used to discriminate water from land features in many applications (Xu, 2006). Instead of a global
229   threshold on the MNDWI, a refined threshold that best divides the specific 'sand' and 'water' pixels
230   by maximizing the inter-class variance is used. It provides a more stable and robust waterline
231   boundary through time (Vos et al., 2019a). A sub-pixel resolution contouring algorithm, referred to as
232   Marching Squares (Cipolletti et al., 2012), is then used to compute and map the waterline W.

233   A CoastSat region was defined at Truc Vert, with Figure 4 showing an example Sentinel-2 satellite
234   image (Figure 4a), the corresponding classified image (Figure 4b), MNDWI pixel values (Figure 4c) and
235   the resulting waterline position. Although a total of 1178 satellite images were available at Truc Vert,
236   many images were not useful. For example, more than half of the images were affected by clouds,
237   which resulted in the automatic removal of 361 images exceeding 50% of cloud cover from the
238   analysis. An additional 339 images were manually removed by visual inspection when the algorithm
239   failed to depict shoreline position for a number of reasons, including: flawed detection of the
240   water/sand limit due to a saturated intertidal domain (Figure 4d) and shadows cast by clouds
241   affecting waterline detection (Figure 4e). Recent Coastsat toolkit development now allows manual
242   adjustment of the waterline by shifting the MNDWI threshold in the MNDWI pixel intensity
243   histogram. However, at the time of using the Coastsat toolkit in the frame of this study, such
244   development was not available but will be addressed in future study. Based on a thorough visual
245   inspection of the images by the operator, a total of 478 Landsat images (including post May 2003 L7
246   images when Scan Line Corrector failed) and Sentinel images (213 since 2009) were therefore used
247   hereafter at Truc Vert representing the period 1984–2019 (Figure 3d).
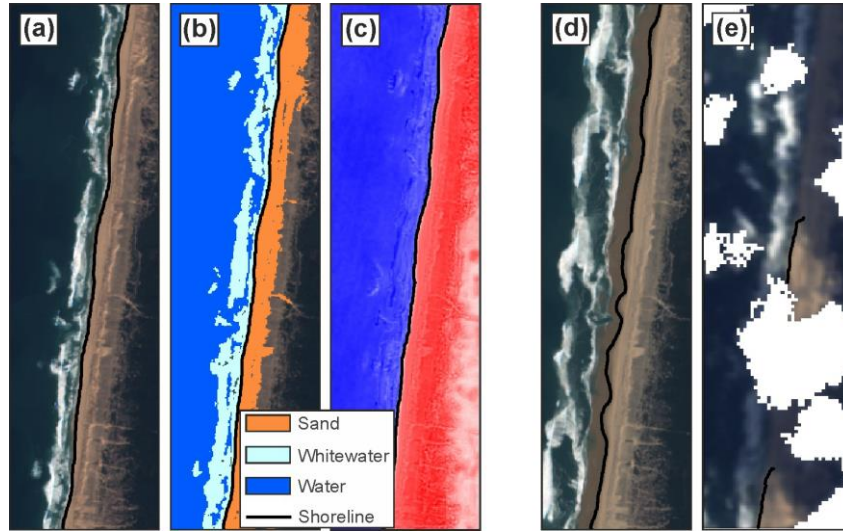
Figure 4. Outputs from the CoastSat tool of Vos (2019b): (a) RGB image of Truc Vert beach from S2 satellite on February 28, 2019; (b) output of image classification where each pixel is labelled as 'sand', 'water', 'white-water' or 'other'; (c) pseudocolor image of the MNDWI pixel values. Examples of images manually disregarded in the analysis: (d) when the algorithm depicted the dry beach limit instead of the waterline due to a saturated intertidal domain (S2 on April 19, 2018); (e) presence of clouds and large casted shadow (L5 on February 23, 1998). In all panels, the black line indicates the waterline detected by CoastSat.

3.4 *Shoreline position computations*

The satellite-derived waterlines were transformed onto the local grid coordinate system. Given that satellite images were taken for a wide range of water levels (Figure 3e) and our interest is in the shoreline position S, waterline positions W were projected to 1.5 m AMSL, which is the most relevant shoreline proxy at Truc Vert as it best correlates with beach-dune volume (Robinet et al., 2016). A water-level correction was applied by translating horizontally the waterline W using a given beach slope m and the water level at the coast η at the satellite flyover time:

$$\Delta y = \frac{\eta - 1.5}{m} \quad (2)$$

where Δy is the cross-shore horizontal shift, positive onshore. The four water-level elevations estimations given in Section 3.2 were tested. In addition, while a constant representative slope for Truc Vert of m = 0.05 was used in line with Vos et al. (2019a), a time- and elevation-dependant slope was also tested here. For the latter, the Truc Vert beach surveys were used to compute the monthly mean beach slope between the 1.5 m AMSL elevation and any elevation along the monthly-mean profile (Figure 5). Beach slope computed from the 1.5 m AMSL elevation to any elevation ranging between -1.5 m and + 3 m AMSL, with end-point slope varying from c. 0.02 to 0.11. Larger slopes are observed at the upper part of the beach during summer, and more gentle slopes during winter and

along the lower part of the profile. Monthly beach slope, however, shows large interannual variability (see large bubbles in Figure 5), particularly during summer at the upper part of the beach.
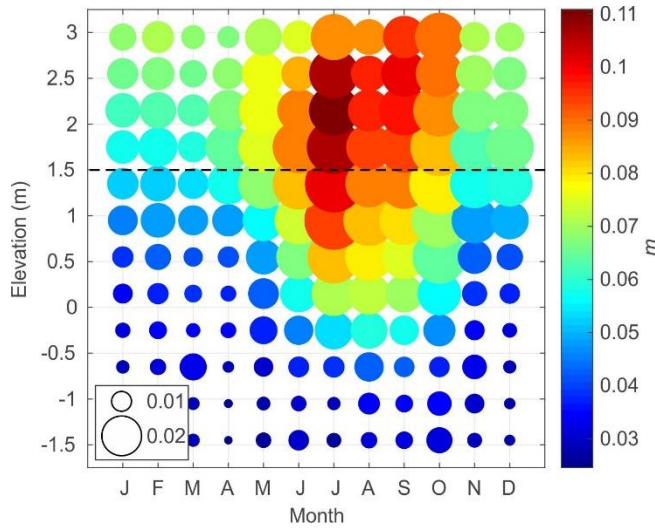

Figure 5. Monthly- and alongshore-averaged beach slope m between a given elevation and the 1.5 m AMSL elevation, with bubble size indicating the monthly standard deviation.

4. Results

4.1 *Waterline detection*

Each satellite-derived waterline, and its cross-shore position $Wsat$, acquired since 2009 was systematically compared with the theoretical waterline (cross-shore position $W\eta$) computed using the Truc Vert beach survey performed closest to the satellite flyover date. For this, all the proxies of water level at the coast η detailed in Section 3.1 were projected on the beach survey. Figure 6 shows an example of the Landsat 8 image taken on November 17, 2014, at 10:48 AM GMT, corresponding to incident waves with H_s = 2.8 m near mid-high tide (η_t = 0.76 m) with negligible non-tidal residuals (< 0.01 m) and large runup ($R_{2\%}$ = 1.73 m). CoastSat detects an alongshore non-uniform waterline depicting megacusp embayments enforced by the inner-bar rip channels (Figure 6a–c). This cuspate morphology is also observed on the closest beach topography, which was surveyed three days later on February 20, 2019. The η_0 (η = 0) elevation iso-contour is located well offshore of the satellite-derived waterline (yellow circles in Figure 6d), on average by c. 70.1 m (Figure 6e). Taking into account the astronomical tide, the η_t elevation iso-contour is located closer to the satellite-derived waterline (Figure 6d), although still well offshore by c. 43.8 m (Figure 6f). Given the negligible non-tidal residuals at the time of this L8 satellite image, the η_{ts} elevation iso-contour essentially superimposes onto that of η_t (Figure 6d,g). In contrast, including wave runup the η_{tsr} elevation iso-contour is translated landward very close to the satellite-derived waterline (Figure 6d), located onshore by c. 2.0 m with an alongshore-averaged root mean square error of 3.7 m (Figure 6h).
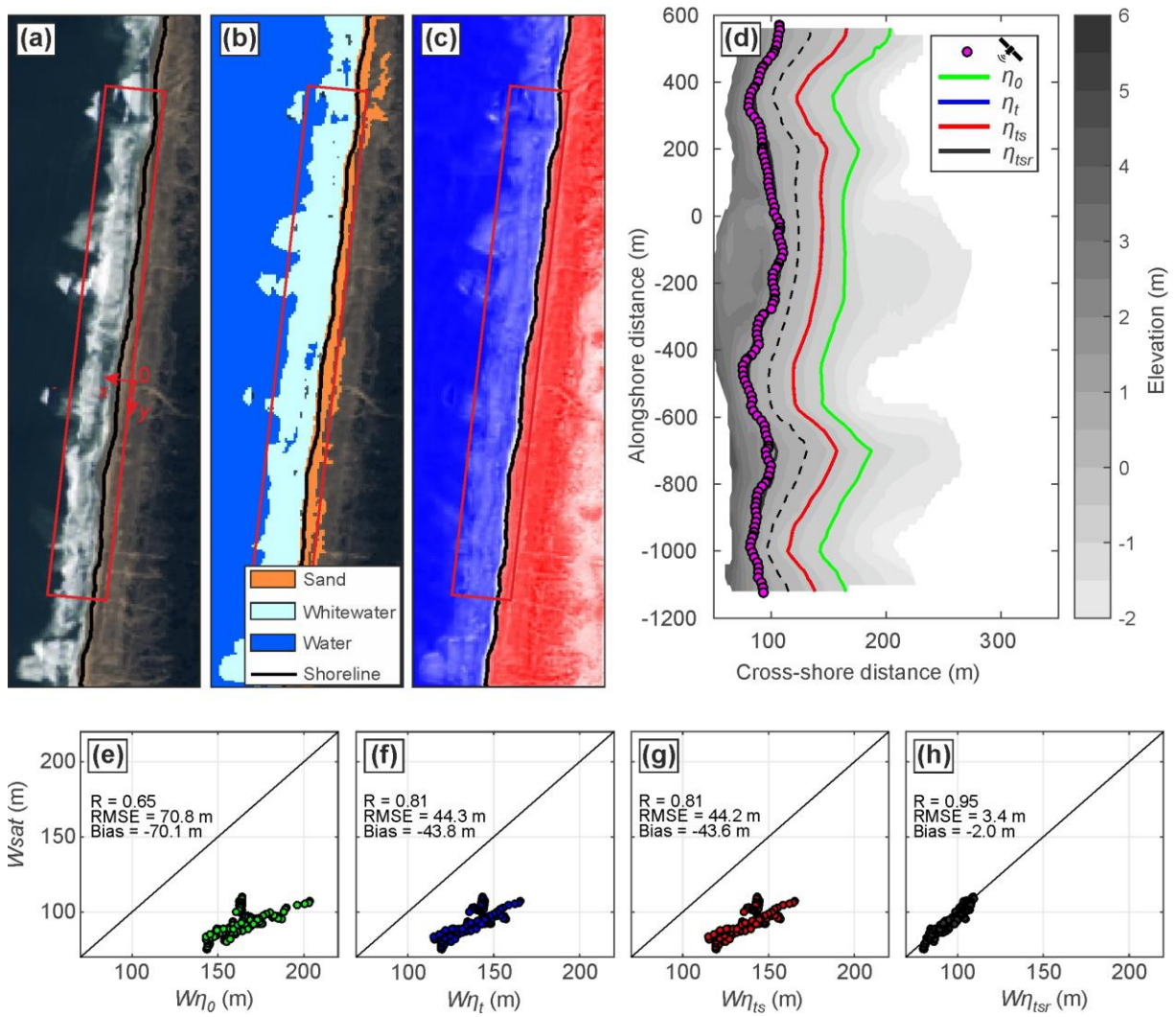
Figure 6. (a-c) Outputs from the CoastSat tool of Vos (2019b) from L8 satellite on November 17, 2014 at 10:48 AM GMT near mid-high tide (η_t = 0.76 m) under energetic waves (H_s = 2.8 m) with (a) RGB image of Truc Vert beach; (b) output of image classification where each pixel is labelled as 'sand', 'water', 'white-water' or 'other'; and (c) pseudocolor image of the MNDWI pixel values. In (a–c), the red box indicates survey region and reference frame used at Truc Vert beach, and the black line indicates the CoastSat waterline. (d) Truc Vert beach topographic survey on November 10, 2014, with AMSL elevation coloured, superimposed waterline points (magenta dots) detected by CoastSat in (a–c) and superimposed iso-contours of elevations: η_0 (0 AMSL), η_t (0.76 m), η_{ts} (0.76 m) and η_{tsr} (2.50 m). Note that the η_t line is hidden behind the η_{ts} line due to negligible non-tidal residual, and that the η_{tsr} line is partly hidden behind the satellite data points. The dashed black line indicates the 1.5-m elevation iso-contour (shoreline proxy at Truc Vert). Comparison of satellite-derived waterline cross-shore positions $Wsat$ against cross-shore positions of iso-contours of elevation (e) η_0, (f) η_t, (g) η_{ts} and (h) η_{tsr} with corresponding correlation (R), root-mean-square error (RMSE) and difference in means (Bias) statistics.

311   Table 1 shows the alongshore-averaged waterline cross-shore position $\overline{W}\eta$ statistics for all usable

312   satellite images since 2009 and for each of the 4 proxies of water level η at the coast. Using all the

313   images since 2009 (n = 226, left-hand column of Table 1), agreement is poor when assuming constant

314   water level at the coast (mean sea level $\overline{W}\eta_0$, R^2 = 0.06, RMSE = 29.0, Bias = -14.9 m). Using

315   astronomical tide ($\overline{W}\eta_t$) improves the agreement (R^2 = 0.60), while adding the atmospheric surge

316   component ($\overline{W}\eta_{ts}$) does not provide further improvement (R^2 = 0.59). In all two situations, the

317   unbiased RMSE (standard deviation STD) and Bias are however still large (STD > 20 m and Bias < -20

318   m). Further adding wave runup to water level iso-contour greatly improves the agreement with

319   CoastSat waterline ($\overline{W}\eta_{ts}$, R^2 = 0.84, STD = 12.4 m, Bias = 3.1 m). Figure 7 further shows that, not

320   surprisingly, errors using η_0 increase as the water level at the time of the satellite flyover deviates

321   from MSL (Figure 7a). In contrast, using astronomical tide ($W\eta_t$), errors are decreased for higher

322   water levels due to steeper beach and small wave height due to smaller runup, say η_{tsr} > 0 and H_s < 1

323   m (Figure 7b), which is the same further adding non-tidal residuals ($\overline{W}\eta_{ts}$, Figure 7c). Finally, further

324   adding wave runup ($\overline{W}\eta_{tsr}$) shows that alongshore-averaged waterline positions are systematically

325   close to that obtained with CoastSat, independent of wave height, for water levels η_{mr} > 0.2 m which

326   is also where the break in slope occurs (Figure 7d). This is reflected in the statistics provided in the

327   middle column of Table1 for (η_{tsr} > 0.2 m, n = 164), showing that, while the coefficient of

328   determination is slightly decreased, STD drops to 7.0 m. A positive Bias is found (7.1 m, Table 1),

329   meaning that the satellite-derived waterline $\overline{W}sat$ is located landward of the theoretical waterline

330     $\overline{W}\eta_{tsr}$, which will be discussed in Section 5. Interestingly, keeping only high-tide images (η_t > 0.5 m

331   like in Vos et al., 2019a, n = 69), only slightly improves the results (right-hand column of Table 1), but

332   more than halves the number of usable images. At the other end (left-hand column of Table 1), using

333   all the images results in larger correlation (R^2 = 0.84) and smaller RMSE (12.8 m). However, STD is

334   almost doubled. These results indicate that, for this study site, using η_{tsr} which includes wave runup

335   and selecting images with η_{tsr} > 0.2 m is the optimal strategy that both minimizes alongshore-

336   averaged waterline position error and maximizes the number of usable satellite images. Finally, it is

337   important to note that these comparisons consider satellite images and beach surveys separated by

338   up to 10 days (Figure 7). Given the large morphological changes occurring at Truc Vert, the errors

339   given here must be considered as conservative.

340   Table 1. Statistics of alongshore-averaged waterline cross-shore positions $\overline{W}\eta$ for each of the 4 water

341   elevation proxies against alongshore-averaged waterline cross-shore position $\overline{W}sat$ computed with

342   CoastSat, using all satellite images, or selecting only those taken for $\eta_{tsr} > 0.2$ m or $\eta_t > 0.5$ m. Only

343   satellite images for which a beach survey was performed within 10 days were considered.

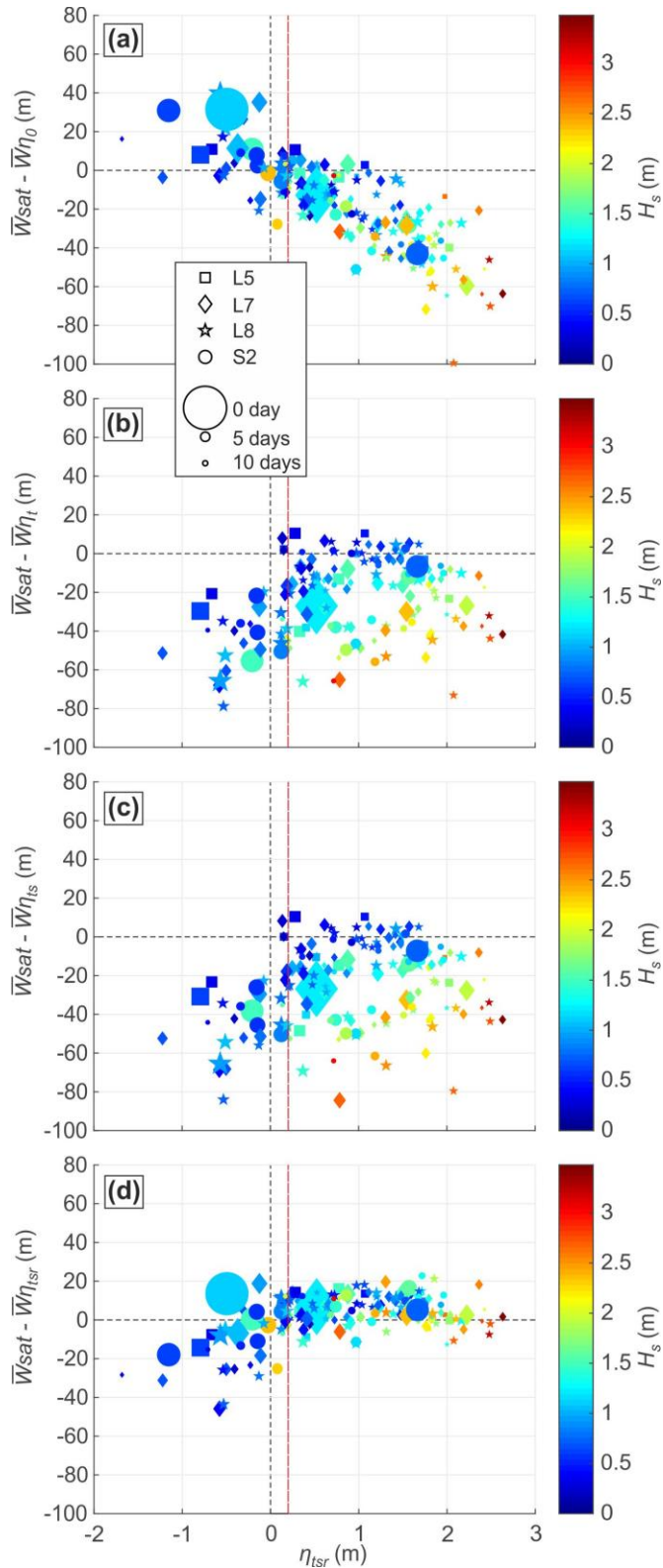|	All (n = 226)			$\eta_{tsr} > 0.2$ m (n = 164)			$\eta_t > 0.5$ m (n = 69)		
	RMSE (STD) [m]	Bias [m]	R^2	RMSE (STD) [m]	Bias [m]	R^2	RMSE (STD) [m]	Bias [m]	R^2
$\bar{W}\eta_0$ (MSL)	29.0 (24.8)	-14.9	0.06	30.7 (17.5)	-24.2	0.05	34.0 (14.1)	-30.9	0.15
$\bar{W}\eta_t$	28.9 (20.2)	-20.7	0.60	23.4 (17.1)	-16.0	0.26	14.5 (12.0)	-8.1	0.28
$\bar{W}\eta_{ts}$	31.4 (21.1)	-23.3	0.59	26.1 (18.7)	-18.2	0.23	15.5 (12.6)	-9.1	0.24
$\bar{W}\eta_{tsr}$	12.8 (12.4)	3.1	0.84	10.0 (7.0)	7.1	0.78	10.6 (6.0)	8.7	0.80

344

345

Figure 7. Difference between alongshore-averaged iso-contour cross-shore position ($\overline{W}\eta$) for

elevations (a) η_0, (b) η_t, (c) η_{ts} and (d) η_{tsr} and alongshore-averaged waterline cross-shore position

computed with CoastSat $\overline{W}sat$, positive meaning more landward satellite-derived waterline, against

estimated total water level η_{tsr}. In all panels, significant wave height H_s is coloured, the vertical

dashed red line indicates the η_{tsr} = 0.2 m threshold, symbol indicates the satellite and symbol size is

351   proportional to the duration between the satellite image and the closest Truc Vert beach

352   topographic survey used to compute iso-contours.

353   **4.2** *Shoreline position*

354   Based on the results of the analysis on the role of water level proxies on the alongshore-averaged

355   waterline cross-shore position $\bar{W}\eta$, and to facilitate comparison with earlier work, only four satellite-

356   derived shoreline position ($S\eta$) methods are further considered by translating horizontally a given

357   waterline $W\eta$ using a given beach slope. Below we now disregard elevation η_{ts} as non-tidal residuals

358   were found to have negligible impact on waterline position at Truc Vert and address four alongshore-

359   averaged shoreline position: (1) $\bar{S}\eta_0$ ignoring tide; (2) $\bar{S}\eta_t$ with tidal correction using water level η_t

360   and a constant slope (m = 0.05 in Equation (2)) as in Vos et al. (2019a); (3) $\bar{S}\eta_{tsr}$ with tidal correction

361   using water level η_{tsr} (i.e. including wave runup) and a constant slope m = 0.05 and (4) $\bar{S}\eta_{tsr\prime}$ with

362   tidal correction using water level η_{tsr} (i.e. including wave runup) and the time- and elevation-varying

363   monthly beach slope shown in Figure 5 feeding Equation (2). Figure 8 shows that the poorest

364   agreement with field data is found for $\bar{S}\eta_0$ (STD = 22.0 m, R^2 = 0.42, Figure 8a), although agreement

365   substantially improves when only considering high-tide images (η_t > 0.5 m; STD = 10.9 m, R^2 = 0.64,

366   Figure 8c). Surprisingly enough, using $\bar{S}\eta_t$ for high-tide images does not further improve the results

367   (Figure 8f). Although a direct comparison cannot be performed, Vos et al. (2019a) who used 74

368   satellite-derived shorelines between 2005-2018 for η_t > 0.5 m at a single transect at Truc Vert, found

369   similar results (STD = 12.7 m, R^2 = 0.46). In contrast, results dramatically improve for $\bar{S}\eta_{tsr}$ (STD = 5.8

370   m, R^2 = 0.86, Figure 8i), meaning that including runup in water level estimation at this coast is key to

371   improve the derived shoreline position. It is important to note that similar agreement is obtained

372   disregarding non-tidal residuals and only including astronomical tide and wave runup (STD = 5.6 m, R^2

373   = 0.86, not shown).

374   Results are not further improved when using a time- and elevation-varying monthly beach slope

375     $\bar{S}\eta_{tsr\prime}$ (STD = 6.6 m, R^2 = 0.81, Figure 8l). This means that, in line with Vos et al. (2019a), further

376   including a presumably better description of beach slope does not necessarily improve the derived

377   shoreline position. While the best results are obtained for $\bar{S}\eta_{tsr}$ for high-tide images, importantly,

378   performance is only marginally less good by including more than twice as many images for η_{tsr} > 0.2

379   m (STD = 7.4 m, R^2 = 0.78 in Figure 8h). Therefore, using $\bar{S}\eta_{tsr}$ appears as the optimal approach to

380   infer shoreline position by both maximizing the number of usable images leading to improved

381   temporal resolution of the shoreline signal and minimizing spatial error associated with the shoreline

382   estimates. Importantly, a substantial positive 7.1 m bias is found, meaning that satellite-derived

383   shoreline is located too far seaward, which will be discussed in Section 5. Disregarding non-tidal

384 residuals and only considering astronomical tide and wave runup ($\bar{S}\eta_{tr}$) gives similar results (STD =

385 7.2 m, $R^2 = 0.78$ for $\eta_{tsr} > 0.2$ m, not shown) to $S\eta_{tsr}$. This emphasizes that astronomical tide and wave

386 runup are key to satellite-derived shorelines, and that, at Truc Vert, non-tidal residuals can be

387 disregarded. Finally, as per the waterline detection, all these errors are considered conservative due

388 to the comparison window (< 10 days between the satellite image the beach survey used for
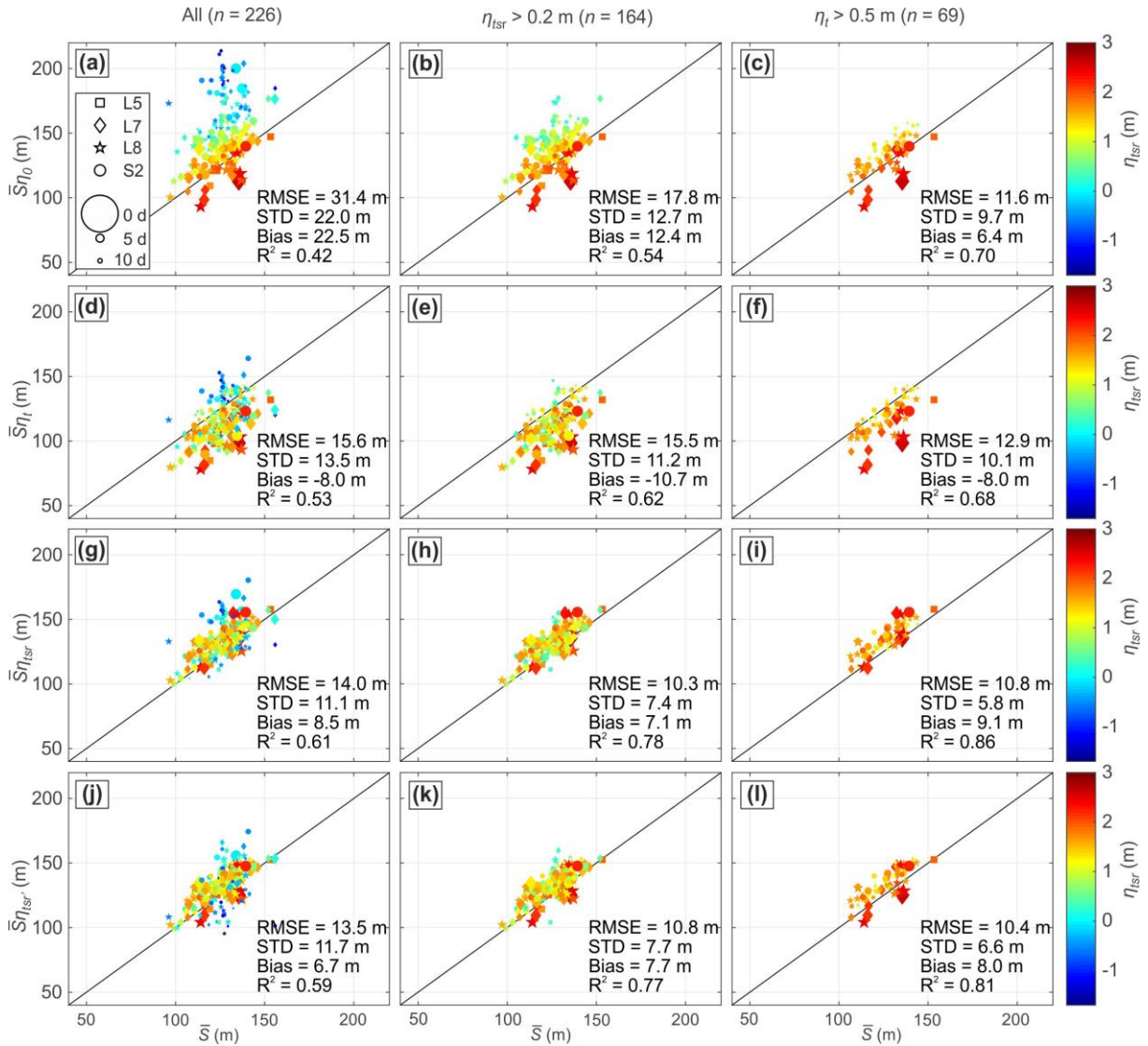
389 comparison).

391 Figure 8. Satellite-derived alongshore-averaged shoreline position against in-situ shoreline position

392 with corresponding statistics using only satellite images for which a beach survey was performed less

393 than 10 days before or after. A positive bias means that satellite-derived shoreline is located too far

394 seaward. The analysis includes (left-hand panels) all usable satellite images since 2009 ($n = 226$);

395 (middle panels) only satellite images for $\eta_{tsr} > 0.2$ m ($n = 164$); and (right-hand panels) only satellite

396 images for $\eta_t > 0.5$ m ($n = 69$). (a–c) $\bar{S}\eta_0$, (d–f) $\bar{S}\eta_t$, (g–i) $\bar{S}\eta_{tsr}$ and (j–l) $\bar{S}\eta_{tsr'}$.

397 **4.3** *Shoreline change analysis: long term trend and interannual variability*

398 Figure 9 shows the time series of alongshore-averaged shoreline position (1.5 m AMSL elevation

399 shoreline proxy) deviation from the mean measured at Truc Vert ($\tilde{S}$) and that derived from satellite

400 images $\tilde{S}\eta_{tsr}$ for images with $\eta_{mr} > 0.2$ m. The satellite-derived shoreline readily reproduces the

401 seasonal and interannual cycles at Truc Vert, despite a few outliers. The computed 2009–2019

402 shoreline trends from measurements and satellite are +0.50 m/yr and +0.57 m/yr, respectively,

403 therefore showing good agreement. Noteworthy, the trend computed using $\tilde{S}\eta_0$ (n = 226) and $\tilde{S}\eta_t$ (n

404 = 69) is 0.81 m/yr and 0.78 m/yr, respectively, which is substantially larger, but of the same order of

405 magnitude as that derived using $\tilde{S}\eta_{tsr}$ (n = 164). Importantly, disregarding non-tidal residuals but

406 keeping runup contribution, 2009-2019 shoreline trend of $\tilde{S}\eta_{tr}$ is 0.63 m/yr, which is closer to that

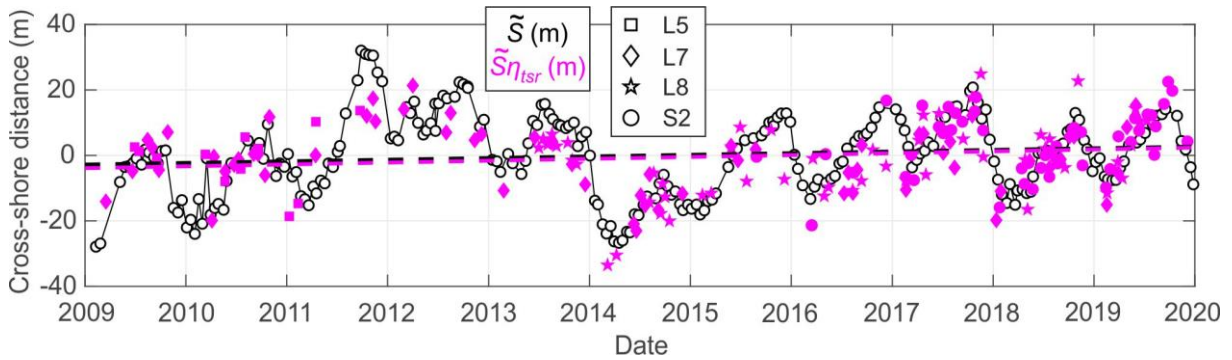407 computed from the topographic surveys.

408

409 Figure 9. Time-series of shoreline change at Truc Vert beach derived from satellite $\tilde{S}\eta_{tsr}$ compared

410 with in-situ shoreline position $\tilde{S}$ with superimposed trends (dashed lines).

411 Figure 10 shows the time series of shoreline deviation from the mean for the entire satellite image

412 dataset, starting from April 21, 1984. Figure 10b shows the results using our optimal approach, which

413 is here disregarding hindcasted non-tidal residuals as they are not available prior to 2006 (and

414 including these did not represent significant improvement anyway). The corresponding $\tilde{S}\eta_{tr}$ long-

415 term trend using images with $\eta_{tr} > 0.2$ m is 0.50 m/yr, which is very similar to that computed for the

416 2009-2019 period (Figure 10a). The long-term trend computed with shoreline $\tilde{S}\eta_0$ is also similar

417 (+0.60 m/yr), while that using $\tilde{S}\eta_t$ for images with $\eta_t > 0.5$ m is slightly reduced (+0.31 m/yr).

418 To emphasize interannual variability, we computed the yearly post-winter mean shoreline position

419 from which we subtracted the long-term trend (coloured bars in Figure 10a). The number of usable

420 satellite images increased in time (Figure 3d) from 2 in 1993 and 1994 to 49 in 2018, and also varied

421 seasonally, ranging from 0.34 images per year in January to 1.91 images in June (related to cloud

422 cover). Therefore, in order to maximize the number of post-winter satellite-derived shoreline

423 positions, we systematically averaged all available shoreline data between April and July. Clearly,

424 strong interannual variability is highlighted, with a typical amplitude of 30–40 m, and with the

425   2013/2014 winter standing out for all shoreline proxies $\tilde{S}\eta_{tr}$ (Figure 10b). Interannual cycles are

426   more pronounced using $\tilde{S}\eta_0$ for all images, with a lot of shoreline outliers (Figure 10a). Interannual

427   cycles for

428     $\tilde{S}\eta_t$ and $\tilde{S}\eta_{tr}$ are more similar in patterns, although using $\tilde{S}\eta_t$ for images with $\eta_t > 0.5$ m does not

429   provide enough post-winter data to address interannual variability prior to the 2000s due to the lack

430   of available images (Figure 10c). Previous work showed that shoreline inter-annual variability on the

431   open beaches of the Atlantic coast of Europe at these latitudes, and particularly at Truc Vert, is

432   strongly affected by the WEPA index (Dodet et al., 2019). A high negative correlation (R = -0.82) was

433   found between post-winter $\tilde{S}\eta_{tr}$ and winter WEPA index, while correlation drops for $\tilde{S}\eta_0$ (R = -0.50)

434   and $\tilde{S}\eta_t$ (R = -0.49). This suggests that interannual shoreline variability can be better depicted using

435     $\tilde{S}\eta_{tr}$ for $\eta_{tr} > 0.2$.
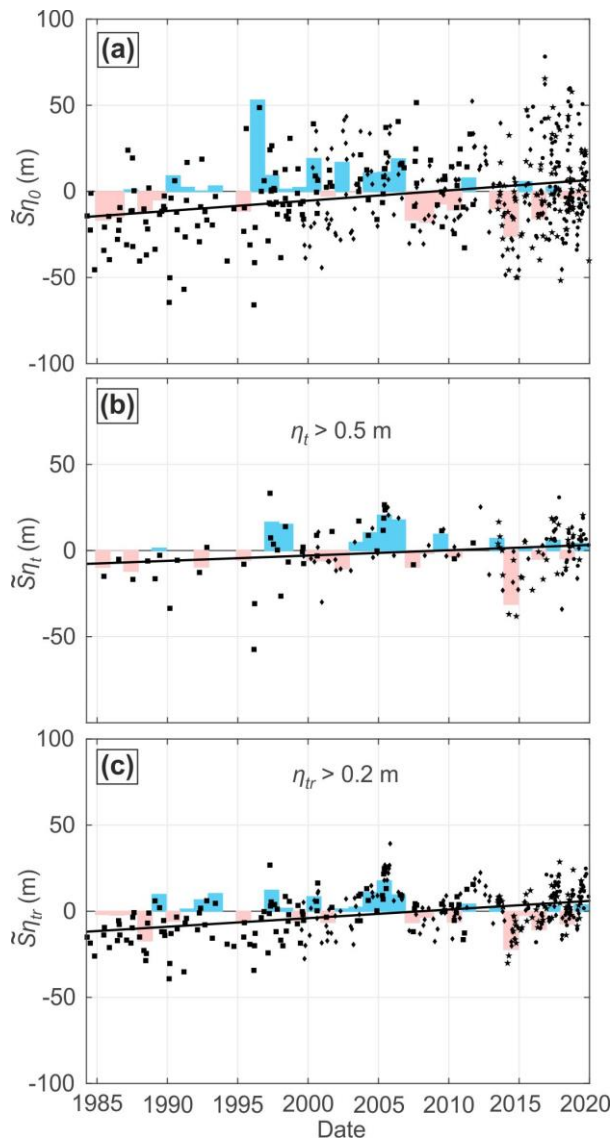

436

437   Figure 10. Time-series of satellite-derived shoreline position deviation from the mean at Truc Vert

438   beach, with the coloured bars showing the interannual variability (trend removed) in post-winter

439 shoreline position and the solid line depicting long-term trend: (a) $\tilde{S}\eta_0$ for all images; (b) $\tilde{S}\eta_t$ for

440 images with $\eta_t > 0.5$ m; (c) $\tilde{S}\eta_{tr}$ for images with $\eta_{tr} > 0.2$ m.

5. Discussion and conclusions

442 Our results indicate that, without having to improve the CoastSat satellite-derived waterline

443 algorithm, the estimation of shoreline position, defined as the profile intersection with a given

444 elevation datum, can be greatly improved on a meso-macrotidal high-energy sandy beach. Crucial to

445 this improvement is accounting for the wave runup. This was surprising as it is highly unlikely that

446 most satellite images were taken at maximum runup excursion. Instead it was expected that the

447 wave set-up, defined by the time-averaged water level of the waterline would be a better descriptor

448 of the shoreline position. However, a preliminary analysis showed that wave set-up only slightly

449 improved waterline detection compared with disregarding wave effects. An explanation for this is

450 that because beaches such as Truc Vert tend to remain wet after the passage of a single runup event,

451 the CoastSat algorithm picks-up the interface between the recent runup (wet) and dry sand instead

452 of the sand/water interface. This may also explain why although the variance in waterline position is

453 largely accounted for by including the wave runup component, the average position of the resulting

454 time- and space-averaged waterline is shifted landward by 7.1 m. (Table 1). Improving the waterline

455 detection for such an environment by using the mean runup instead of the 2% exceedance runup

456 ($R_{2\%}$) will need further investigation. We also tested other set-up and runup formulas, which did not

457 yield better results. For instance, the formulation used here by Sénéchal et al. (2011) resulted in a

458 substantially large inshore bias (runup overestimation) of waterline position compared to other

459 formulas, meaning that runup elevations are possibly overestimated. However, this formulation

460 provided the best variance explanation, which is why it was preferred therein. For instance, using

461 images with $\eta_{tsr} > 0.2$ m, waterline STD and R^2 are 7.0 m and 0.78 (Table 1), respectively. Results

462 worsen using the runup parametrizations proposed by Stockdon at al. (2006) for intermediate and

463 dissipative beaches, with STD = 8.8 m and R^2 = 0.67 for the intermediate beach parametrization, and

464 with STD = 8.7 m and R^2 = 0.67 for the dissipative parametrization. However, waterline estimation

465 using Stockdon et al. (2006) is still greatly improved compared with when wave contribution to water

466 level at the coast is disregarded ($\overline{W}\eta_0$ and $\overline{W}\eta_t$ in Table 1). Our new approach also allows using a

467 lower water level threshold ($\eta_{tsr} > 0.2$ m), greatly increasing the number of useable images available

468 for shoreline change analysis. This improvement is especially important for higher latitudes where

469 more frequent cloud cover significantly reduces the number of cloud-free images. However, this

470 threshold is likely site specific and does not correspond to any salient break in beach slope at Truc

471 Vert. Environmental factors controlling this threshold will need to be addressed by exploring

472 satellite-derived shoreline at other beaches where beach profiles are regularly surveyed.

473   Including the non-tidal water level residuals did not improve the results at Truc Vert. However, this is

474   not a generic result as at Truc Vert, and along the entire Aquitaine coast studied here (Figure 1a), the

475   atmospheric surge is quite small (Le Cann, 1990) owing to the quite narrow continental shelf.

476   Atmospheric surge at Truc Vert at all the satellite flyover dates used here ranged from -0.27 m to

477   +0.29 m with a mean of -0.05 m (Figure 3e). This is small compared to the wave runup, ranging from

478   0.17 m to 1.89 m with a mean of 0.91 m (Figure 3f), and the meso-macrotidal tide range (Figure 3e).

479   However, including storm surge may be critical to improve shoreline estimation on coasts with small

480   tide range, but potentially large surge due to large and shallow continental shelf. For instance, sea

481   level can rise by metres due to atmospheric surge in the North Sea (Spencer et al., 2015), the Gulf of

482   Mexico (Sheng et al., 2004) or even c. 100 km north of the study area where the continental shelf

483   becomes much wider and shallower (Bertin et al., 2012). For energetic coasts with similar settings as

484   Truc Vert, overlooking atmospheric surge is acceptable, which is an advantage for practical

485   applications as accurate local surge hindcasts starting back in the 80s are scarce.

486   Another important parameter to quantify is the beach slope, which is used in traditional set-up and

487   runup formulas (Stockdon et al., 2006) and for tidal correction (Vos et al., 2019a). Nevertheless, using

488   a time- and space-varying slope does not improve shoreline reconstruction for Truc Vert, which is

489   another advantage for practical application as only an average beach slope value needs to be

490   provided. Recently, Vos et al. (2020) developed a simple and efficient approach to derive beach slope

491   from the same publicly available satellite images, making it possible to compute satellite shoreline

492   position without requiring local topographic data.

493   Our work has therefore identified key parameters contributing to shoreline error reduction through

494   the development of a robust methodology. These improvements need to be tested at other sites, in

495   particular on reflective gravel and mixed sand-gravel beaches, and ultra-dissipative sandy mega-tidal

496   beaches. Further possibility for uncertainty reduction concerns the georeferencing and the better

497   detection of the sand/water interface. The CoastSat waterline detection algorithm uses an image

498   classification based on a Neural Network trained at five beaches along the New South Wales coast

499   (Vos et al., 2019a). Training a new Neural Network for more representative sites may further improve

500   the sand/water interface detection. Overall, more work is required to identify and further address

501   other key sources of uncertainties, which is beyond the scope of the present paper.

502   The 35-year shoreline time series at Truc Vert (1984–2019) shows that more accurate assessment of

503   long-term shoreline trends and interannual variability can be computed than was achieved in

504   previous global studies (e.g., Luijendijk et al., 2018; Mentaschi et al., 2018). Similar trends are

505   obtained with $\tilde{S}\eta_{tr}$ (+0.50 m/yr) and $\tilde{S}\eta_0$ (+0.60 m/yr) (Figure 10b). However, shoreline trend

506 computation at other sites along the Aquitaine coast (e.g. Hourtin, Biscarrosse, Figure 1a) indicates

507 that much larger differences can be observed. $\tilde{S}\eta_0$, which does not account for water level

508 fluctuations, is close to the global approach in Luijendijk et al. (2018) who used yearly composite and

509 therefore averaged water level variations. A detailed inspection of the trends computed in Luijendijk

510 et al. (2018) at Truc Vert shows trends that are very different to those computed herein. The

511 dominant trend computed by Luijendijk et al. (2018) at Truc Vert indicates, strongly alongshore

512 variable, large, erosion at -1.13 m/yr averaged over the same 3500-m sector, peaking locally at 3.8

513 m/yr. A strong alongshore variability was also found in Mentaschi et al. (2018), although a direct

514 quantitative comparison could not be performed. This goes against decadal and multi-decadal

515 observations at this coast (e.g., Castelle et al., 2017a, 2018) and results presented herein, which all

516 concur to an alongshore-uniform c. +0.5 m/yr trend. It must be acknowledged that the comparison

517 above is performed between a site-specific analysis where the images were manually selected and a

518 runup correction was applied using a local wave and water level hindcast (our study), and a global

519 method that was applied over the whole world (Luijendijk et al., 2018; Mentaschi et al., 2018).

520 We therefore anticipate that the new approach proposed here can improve the accuracy of satellite

521 shoreline long-term trends and interannual variability along many coasts worldwide. However, at

522 rapidly evolving sections, improvements will be marginal. North of Truc Vert, at Cape Négade (Figure

523 1a), the long-term trend is reasonably steady at -4.63 m/yr for $\tilde{S}\eta_{tr}$ (Figure 11a-e), and is very similar

524 with all the other shoreline proxies (not shown). The same applies further south at the tip of the Cap

525 Ferret sand spit or at La Salie at each side of the Arcachon Lagoon tidal inlet, where large long-term

526 trends of +3.34 m/yr and -8.38 m/yr are computed, respectively. However, large cycles are observed

527 with some dramatic decadal trends. For instance, the shoreline at La Salie has been eroding by nearly

528 30 m/yr over the last seven years (Figure 11k), despite an overall positive shoreline trend since the

529 1980s. Therefore, except at Cape Négade, where chronic erosion is relatively steady, further

530 extrapolating these 35-year trends to estimate shoreline position by 2100 (Vousdoukas et al., 2020)

531 is questionable, because time scales of shoreline cycles are similar to the period of satellite data
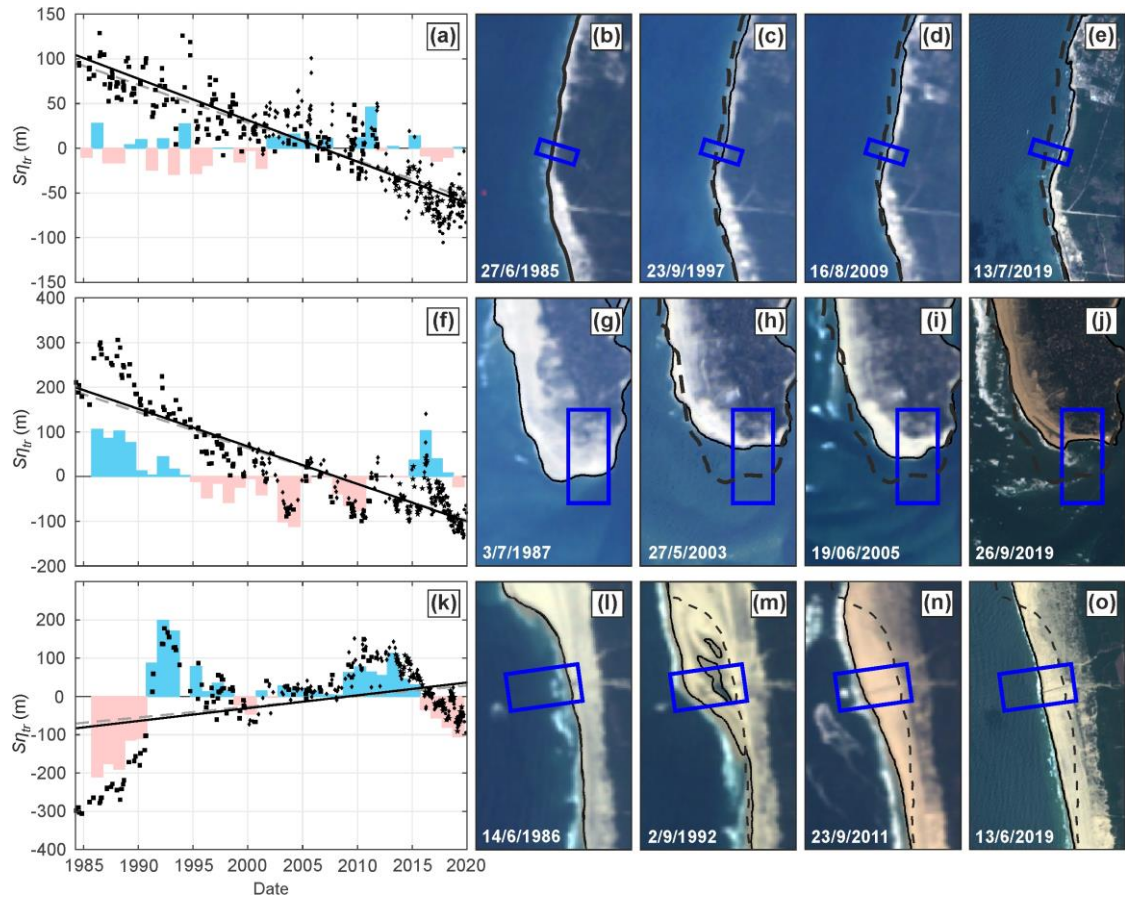
532 availability.

Figure 11. Left-hand panels: time series of shoreline position at (a) Cape Négade, (f) Cap Ferret sandspit tip and (k) la Salie (see location map in Figure 1a) derived from satellite $\tilde{S}\eta_{tr}$. In the left-hand panels the linear shoreline trend for $\tilde{S}\eta_{tr}$ is indicated by the black dotted line. The coloured bars in (a,b) show the inter-annual variability (trend removed) in post-winter shoreline position. Right-hand panels: corresponding RGB images at different relevant stages of evolution, blue boxes indicate areas where shoreline positions were averaged alongshore to compute the time series shown in the left-hand panels.

We acknowledge that the concept of global application is very attractive and responds to strong demand. However, past shoreline trends estimations on beaches incurs large uncertainties, which become exacerbated if extrapolated in time to estimate future shoreline change. Vos et al. (2019a) recognised issues with dissipative and large tidal range sites. This work has identified key parameters contributing to large errors for this type of environment and developed a robust methodology for limiting uncertainty. Such approach requires accurate tide and inshore wave hindcasts, which can be challenging to obtain in complex coastal settings where, e.g., wave shadowing from offshore islands or offshore wave refraction can largely impact breaking wave conditions. These improvements need to be tested in other sites with similar tidal/wave forcing characteristics but different morphological and sediment characteristics. This will allow addressing the links between coastal response and large-

scale climate patterns of atmospheric variability in a wide range of environments. It will also provide improved beach state classification and, where time scales of shoreline cycles are not similar to the period of data availability (e.g. away from inlet and estuary mouths), less uncertain shoreline projections by the end of the century in the context of climate change.

Acknowledgments

References cited

Almar, R., Castelle, B., Ruessink, B.G., Sénéchal, N., Bonneton, P., Marieu, V., 2010. Two- and three-dimensional double-sandbar system behaviour under intense wave forcing and a meso-macro tidal range. Continental Shelf Research, 30, 781-792.

Baptista, P., Bastos, L., Bernardes, C., Cunha, T., Dias, J., 2008. Monitoring Sandy Shores Morphologies by DGPS—A Practical Tool to Generate Digital Elevation Models. Journal of Coastal Research, 24, 1516–1528, doi:10.2112/07-0861.1.

Bertin, X., Bruneau, N., Breilh, J.F., Fortunato, A.B., Karpytchev, M., 2012. Importance of wave age and resonance in storm surges: The case Xynthia, Bay of Biscay. Ocean Modelling, 42, 16-30, doi:10.1016/j.ocemod.2011.11.001.

Boudière, E., Maisondieu, C., Ardhuin, F., Accensi, M., Pineau-Guillou, L., Lepesqueur, J., 2013. A suitable metocean hindcast database for the design of Marine energy converters. International Journal of Marine Energy, 3–4, 40-52, doi:10.1016/j.ijome.2013.11.010

Carter, R.W.G., Johnston, T.W., McKenna, J., Orford, J.D., 1987. Sea-level, sediment supply and coastal changes: Examples from the coast of Ireland. Progress In Oceanography, 18(1-4), 79-101.

583 Castelle, B., Bonneton, P., Dupuis, H., Sénéchal, N., 2007. Double bar beach dynamics on the high-
584   energy meso-macrotidal French Aquitanian Coast: a review. Marine Geology, 245, 141-159.

585 Castelle, B., Marieu, V., Bujan, S., Ferreira, S., Parisot, J.P., Capo, S., Senechal, N., Chouzenoux, T.,
586   2014. Equilibrium shoreline modelling of a high-energy meso-macrotidal multiple-barred
587   beach. Marine Geology, 347, 85–94.

588 Castelle, B., Bujan, S., Ferreira, S., Dodet, G., 2017a. Foredune morphological changes and beach
589   recovery from the extreme 2013/2014 winter at a high-energy sandy coast. Marine Geology,
590   385, 41-55.

591 Castelle, B., Dodet, G., Masselink, G., Scott, T., 2017b. A new climate index controlling winter wave
592   activity along the Atlantic coast of Europe: The West Europe Pressure Anomaly. Geophysical
593   Research Letters, 44 (3), 1384-1392.

594 Castelle, B., Guillot, B., Marieu, V., Chaumillon, E., Hanquiez, V., Bujan, S., Poppeschi, C., 2018. Spatial
595   and temporal patterns of shoreline change of a 280-km long high-energy disrupted sandy
596   coast from 1950 to 2014: SW France. Estuar. Coast. Shelf Sci. 200, 212–223.

597 Castelle, B., Marieu, V., Bujan, S., Ferreira, S., 2020. 16 years of topographic surveys of rip-channelled
598   high-energy meso-macrotidal sandy beach. Scientific Data, 7, 410, doi:10.1038/s41597-020-
599   00750-5.

600 Cipolletti, M.P., Delrieux, C.A., Perillo, G.M.E., Cintia Piccolo, M., 2012. Superresolution border
601   segmentation and measurement in remote sensing images. Comput. Geosci., 40, 87–96,
602   doi:10.1016/j.cageo.2011.07.015.

603 Cooper, J. A.G., Masselink, G., Coco, G., Short, A.D., Castelle, B., Rogers, K., Anthony, E., Green, A.N.,
604   Kelley, J.T., Pilkey, O.H., Jackson, D.W.T., 2020. Sandy beaches can survive sea-level rise.
605   Nature Climate Change, 10 (11), 993-995, doi:10.1038/s41558-020-00934-2.

606 D'Anna, M., Castelle, B., Idier, D., Le Cozannet, G., Rohmer, J., Robinet, A., 2020. Impact of model free
607   parameters and sea-level rise uncertainties on 20-years shoreline hindcast: the case of Truc
608   Vert beach (SW France). Earth Surface Processes and Landforms, 45(8), 1895-1907,
609   doi:10.1002/esp.4854

610 Dodet, G., Castelle, B., Masselink, G., Scott, T., Davidson, M., Floc'h, F., Jackson, D.W.T., Suanez, S.,
611   2019. Beach recovery from extreme storm activity during the 2013/14 winter along the
612   Atlantic coast of Europe. Earth Surface Processes and Landforms, 44(1), 393-401.

613 Duarte, C.R., De Miranda, F.P., Landau, L., Souto, M.V.S., Sabadia, J.A.B., Da Silva, C.A., Rodrigues,
614   L.I.D.C., Damasceno, A.M., 2018. Short-time analysis of shoreline based on RapidEye satellite
615   images in the terminal area of Pecem Port, Ceara, Brazil. International Journal of Remote
616   Sensing, 39, 4376-4389.

617   Gallagher, E.L., MacMahan, J.H., Reniers, A.J.H.M., Brown, J., Thornton, E.B., 2011. Grain size
618   variability on a rip-channeled beach. Marine Geology 1-4, 43–53.

619   Garcia-Rubio, G., Huntley, D., Russell, P., 2015. Evaluating shoreline identification using optical
620   satellite images. Marine Geology, 359, 96-105, doi:10.1016/j.margeo.2014.11.002.

621   Harley, M.D., Turner, I.L., Short, A.D., Ranasinghe, R., 2011. Assessment and integration of
622   conventional, RTK-GPS and image-derived beach survey methods for daily to decadal coastal
623   monitoring. Coastal Engineering 58, 194–205.

624   Harley, M.D., Turner, I.L., Kinsela, M.A., Middleton, J.H., Mumford, P.J., Splinter, K.D., Phillips, M.S.,
625   Simmons, J.A., Hanslow, D.J., Short, A.D., 2017. Extreme coastal erosion enhanced by
626   anomalous extratropical storm wave direction. Scientific Reports, 7: 6033.

627   Hurrell, J.W., 1995. Decadal Trends in the North Atlantic Oscillation: Regional Temperatures and
628   Precipitation. Science, 269, 676-679.

629   Ibaceta, R., Splinter, K.D., Harley, M.D., & Turner, I.L., 2020. Enhanced Coastal Shoreline Modeling
630   Using an Ensemble Kalman Filter to include Nonstationarity in Future Wave Climates.
631   Geophysical Research Letters, 47(22), doi.org/10.1029/2020GL090724

632   Laporte-Fauret, Q., Marieu, V., Castelle, B., Michalet, R., Bujan, S., Rosebery, D., 2019. Low-Cost UAV
633   for High-Resolution and Large-Scale Coastal Dune Change Monitoring Using
634   Photogrammetry. Journal of Marine Science Engineering, 7:63, doi: 10.3390/jmse7030063.

635   Le Cann, B., 1990. Barotropic tidal dynamics of the Bay of Biscay shelf: observations, numerical
636   modelling and physical interpretation. Continental Shelf Research, 10 (8), 723–758.

637   Lee, G.H., Nicholls, R.J., Birkemeier, W.A., 1998. Storm-driven variability of the beach-nearshore
638   profile at Duck, North Carolina, USA, 1981–1991. Mar. Geol. 148 (3), 163–177.

639   Le Mauff, B., Juigner, M., Ba, A., Robin, M., Launeau, P., Fattal, P., 2018. Coastal monitoring solutions
640   of the geomorphological response of beach-dune systems using multi-temporal LiDAR
641   datasets (Vendée coast, France), Geomorphology, 304,121-140, doi
642   :10.1016/j.geomorph.2017.12.037.

643   Liu, Q., Trinder, J., Turner, I.L., 2017. Automatic super-resolution shoreline change monitoring using
644   Landsat archival data: a case study at Narrabeen–Collaroy Beach, Australia. Journal of
645   Applied Remote Sensing, 11, 016036, doi:10.1117/1.JRS.11.016036.

646   Luijendijk, A., Hagenaars, G., Ranasinghe, R., Baart, F., Donchyts, G., Aarninkhof, S., 2018. The State
647   of the World's Beaches. Scientific Reports, 8(1), doi:10.1038/s41598-018-24630-6.

648   Ludka, B.C., Guza, R.T., O'Reilly, W.C., Merrifield, M.A., Flick, R.E., Bak, A.S., Hesser, T., Bucciarelli, R.,
649   Olfe, C., Woodward, B., Boyd, W., Smith, K., Okihiro, M., Grenzeback, R., Parry, L., Boyd,
650   G.,2019. Sixteen years of bathymetry and waves at San Diego beaches. Sci Data 6, 161,
651   doi:10.1038/s41597-019-0167-6.

652 McCarroll, R.J., Masselink, G., Valiente, N.G., Scott, T., Wiggins, M., Kirby, J., Davidson, M., 2020. A
653   novel rules-based shoreface translation model for predicting future coastal change:
654   ShoreTrans. Doi:10.31223/osf.io/y4kmv

655 Masselink, G., Castelle, B., Scott, T., Dodet, G., Suanez, S., Jackson, D., Floc'h, F., 2016. Extreme wave
656   activity during 2013/2014 winter and morphological impacts along the Atlantic coast of
657   Europe. Geophysical Research Letters, 43, 2135-2143, doi: 10.1002/2015GL067492.

658 Mentaschi, L., Vousdoukas, M.I., Pekel, J.-F., Voukouvalas, E., Feyen, L., 2018. Global long-term
659   observations of coastal erosion and accretion. Scientific Reports, 8, 12876,
660   doi:10.1038/s41598-018-30904-w.

661 Michaud, H., Pasquet, A., Baraille, R., Leckler, F., Aouf, L., Dalphinet, A., Huchet, M., Roland, A.,
662   Dutour-Sikiric, M., Ardhuin, F., Filipot, J.F, 2015. Implementation of the new French
663   operational coastal wave forecasting system and application to a wave-current interaction
664   study. 14th International Workshop on Wave Hindcasting and Forecasting & 5th Coastal
665   Hazard Symposium, Nov. 8-13, Key West, Florida, USA.

666 Nicolae-Lerma, A., Ayache, B., Ulvoas, B., Paris, F., Bernon, N., Bultreau, T., Mallet, C., 2019.
667   Pluriannual beach-dune evolutions at regional scale: Erosion and recovery sequences analysis
668   along the Aquitaine coast based on airborne LiDAR data. Continental Shelf Research. 189,
669   103974.

670 O'Connor, M.C., Cooper, J.A.G., Jackson, D.W.T., 2017. Decadal behavior of tidal inlet–associated
671   beach systems, Northwest Ireland, in relation to climate Forcing. Journal of Sedimentary
672   Research, 81 (1), 38–51. doi: 10.2110/jsr.2011.3.

673 Pianca, C., Holman, R.A., Siegle, E., 2015. Shoreline variability from days to decades: Results of long-
674   term video imaging. Journal of Geophysical Research-Oceans, 120, 2159–2178.

675 Pineau-Guillou, L., 2013. PREVIMER. Validation des modèles hydrodynamiques 2D des côtes de la
676   Manche   et   de   l'Atlantique.   ODE/DYNECO/PHYSED/2013-05.
677   https://archimer.ifremer.fr/doc/00157/26800/

678 Qiao, G., Mi, H., Wang, W., Tong, X., Li, Z., Li, T., Liu, S., Hong, Y., 2018. 55-year (1960–2015)
679   spatiotemporal shoreline change analysis using historical DISP and Landsat time series data in
680   Shanghai, International Journal of Applied Earth Observation, 68, 238-251, doi:
681   10.1016/j.jag.2018.02.009.

682 Ranasinghe, R., Callaghan, D. Stive, M.J.F., 2012. Estimating coastal recession due to sea level rise:
683   beyond the Bruun rule. Clim. Chan., 110, 561-574.

684 Robinet, A., Castelle, B., Idier, D., Le Cozannet, G., Déqué, M., Charles, E., 2016. Statistical modeling
685   of interannual shoreline change driven by North Atlantic climate variability spanning 2000-
686   2014 in the Bay of Biscay. Geo-Marine Letters, 36, 479-490.

687   Ruessink, B.G., Kleinhans, M.G., Van den Beukel, P.G.L., 1998. Observations of swash under highly
688   dissipative conditions. Journal of Geophysical Research, 103, 3111-3118.

689   Ruggiero, P., Komar, P.D., Marra, J.J., McDougal, W.G., Beach, R.A., 2001. Wave runup, extreme
690   water levels and the erosion of properties backing beaches. Journal of Coastal Research, 17,
691   407-419.

692   Schubert, A., Miranda, N., Geudtner, D., Small, D., 2017. Sentinel-1A/B Combined Product
693   Geolocation Accuracy. Remote Sensing, 9(6), 607, doi:10.3390/rs9060607.

694   Senechal, N., Coco, G., Bryan, K.R., and Holman, R.A., 2011. Wave runup during extreme storm
695   conditions, Journal of Geophysiscal Research, 116, C07032, doi:10.1029/2010JC006819.

696   Sheng, Y.P., Zhang, Y., Paramygin, V.A., 2004. Simulation of storm surge, wave, and coastal
697   inundation in the Northeastern Gulf of Mexico region during Hurricane Ivan in 2004. Ocean
698   Modelling, 35(4), 314-331, doi:/10.1016/j.ocemod.2010.09.004.

699   Spencer, T., Brooks, S.M., Evans, B.R., Tempest, J.A., Möller, I., 2015. Southern North Sea storm surge
700   event of 5 December 2013: Water levels, waves and coastal impacts. Earth-Science Reviews,
701   146, 120-145, doi:10.1016/j.earscirev.2015.04.002.

702   Splinter, K., Turner, I.L., Davidson, M.A., 2013. How much data is enough? The importance of
703   morphological sampling interval and duration for calibration of empirical shoreline models.
704   Coastal Engineering, 77, 14-27, doi:10.1016/j.coastaleng.2013.02.009

705   Splinter, K.D., Turner, I.L., Davidson, M.A., Barnard, P., Castelle, B., Oltman-Shay, J., 2014. A
706   generalized equilibrium model for predicting daily to interannual shoreline response. Journal
707   of Geophysical Research - Earth Surface, 119, 1936–1958, doi:10.1002/2014JF003106.

708   Stive, M.J.F., Aarninkhof, S.G.J., Hamm, L., Hanson, H., Larson, M., Wijnberg, K.M., Nicholls, R.J.,
709   Capobianco, M., 2002. Variability of shore and shoreline evolution. Coastal Engineering,
710   47(2), 211-235, doi:10.1016/S0378-3839(02)00126-6.

711   Stockdon, H.F., Holman, R.A., Howd, P.A., Sallenger, A.H., 2006. Empirical parameterization of setup,
712   swash, and runup. Coastal Engineering, 53, 573–588, doi:10.1016/j.coastaleng.2005.12.005.

713   Stokes, C., Davidson, M. Russell, P., 2015. Observation and prediction of three-dimensional
714   morphology at a high-energy macrotidal beach. Geomorphology 243, 1–13.

715   Suanez, S., Cariolet, J.M., Cancouët, R., Ardhuin, F., Delacourt, C., 2012. Dune recovery after storm
716   erosion on a high-energy beach: Vougot Beach, Brittany (France). Geomorphology, 139–140,
717   16-33, doi:10.1016/j.geomorph.2011.10.014.

718   Toimil, A., Camus, P., Losada, I.J., Le Cozannet, G., Nicholls, R., Idier, D., Maspataud, A., 2020. Climate
719   change-driven coastal erosion modelling in temperate sandy beaches methods and
720   uncertainty   treatment.   Earth   Science   Reviews,   202,   103110,
721   doi:10.1016/j.earscirev.2020.103110.

722   Toure, S., Diop, O., Kpalma, K., Maiga, A.S., 2019. Shoreline Detection using Optical Remote Sensing:
723   A Review. ISPRS Int. J. Geo-Inf., 8(2), 75, doi:10.3390/ijgi8020075.

724   Turner, I.L., 2006. Discriminating Modes of Shoreline Response to Offshore-Detached Structures.
725   Journal of Waterway, Port, Coastal, and Ocean Engineering, 132(3), 180-191.

726   Turner, I.L., Harley, M.D., Short, A.D., Simmons, J.A., Bracs, M.A., Phillips, M.S., Splinter, K.D., 2016. A
727   multi-decade dataset of monthly beach profiles and inshore wave forcing at Narrabeen,
728   Australia. Scientific Data, 2, 160024.

729   Vitousek, S., Barnard, P.L., Limber, P., Erikson, L., Cole, B., 2017. A model integrating longshore and
730   cross-shore processes for predicting long-term shoreline response to climate change. Journal
731   of Geophysical Research Earth Surface, 122, 782– 806, doi:10.1002/2016JF004065.

732   Vos, K., Harley, M.D., Splinter, K.D., Simmons, J.A., Turner, I.L., 2019a. Sub-annual to multi-decadal
733   shoreline variability from publicly available satellite imagery. Coastal Engineering,
734   doi:10.1016/j.coastaleng.2019.04.004.

735   Vos, K., Splinter, K.D., Harley, M.D., Simmons, J.A., Turner, I.L., 2019b. CoastSat: A Google Earth
736   Engine-enabled Python toolkit to extract shorelines from publicly available satellite imagery.
737   Environmental Modelling & Software, 122, 104528, doi:10.1016/j.envsoft.2019.104528.

738   Vos, K., Harley, M.D., Splinter, K.D., Walker, A., Turner, I.L., 2020. Beach Slopes From Satellite-Derived
739   Shorelines. Geophysical Research Letters, 47, e2020GL088365, doi:10.1029/2020GL088365

740   Vousdoukas, M.I., Ranasinghe, R., Mentaschi, L., Plomaritis, T.A., Athanasiou, P., Luijendyk, A., Feyen,
741   L., 2020. Sandy Beaches under threat of erosion. Nature Climate Change, 10, 260-263,
742   doi:10.1048/s41558-020-0697-0.

743   Wijnberg, K.M. & Terwindt, J.H., 1995. Extracting decadal morphological behaviour from high-
744   resolution, long-term bathymetric surveys along the Holland coast using eigenfunction
745   analysis. Marine Geology 126, 301–330.

746   Wiggins, M., Scott, T., Masselink, G., Russell, P., McCarroll, R.J., 2019. Coastal embayment rotation:
747   Response to extreme events and climate control, using full embayment surveys.
748   Geomorphology, 327, 385-403, doi:10.1016/j.geomorph.2018.11.014.

749   Xu, H., 2006. Modification of normalised difference water index (NDWI) to enhance open water
750   features in remotely sensed imagery. Int. J. Remote Sens. 27, 3025–3033,
751   doi:10.1080/01431160600589179.